Ligand Tail Controls the Conformation of Indium Sulfide Ultrathin Nanoribbons

Lilian Guillemeney, Sarit Dutta, Rodolphe Valleix, Gilles Patriarche, Benoît Mahler, Benjamin Abécassis

Ligand Tail Controls the Conformation of Indium Sulfide ultrathin nanoribbons

Lilian Guillemeney,[1] Sarit Dutta,[2] Rodolphe Valleix,[2] Gilles Patriarche,[3] Benoit Mahler,[4] and Benjamin Abécassis*[2]

[1] *ENS de Lyon, CNRS, LCH, UMR 5182, 69342, Lyon cedex 07, France*
[2] *CNRS, ENS de Lyon, LCH, UMR 5182, 69342, Lyon cedex 07, France*
[3] *Centre de Nanosciences et de Nanotechnologies, CNRS, Université Paris Saclay, 91120 Palaiseau, France*
[4] *CNRS, UCBL, ILM, UMR 5306, 69622 Villeurbanne, France*

(Dated: July 11, 2024)

We report the conformational control of 2D ultra-thin indium sulfide nanoribbons by tuning their amine ligands' alkyl chain. The initial orthorhombic InS nanoribbons bare *n*-octylamine ligands and display a highly curved geometry with a characteristic figure of eight shapes. Exchanging the native ligand by oleylamine induces their complete unfolding to yield flat board-shaped nanoribbons. Significant strain variations in the InS crystal structure accompany this shape-shifting. By tuning the linear alkyl chain length from 4 to 18 carbon atoms, we show using SAXS in solution and TEM that the curvature of the nanoribbon subtly depends on the ligand-ligand interactions at the nanoribbon's surface. The curvature decreases gradually as the chain length increases, while carbon unsaturation has an unexpectedly significant effect at constant chain length. These experiments shed light on the critical role of the ligand monolayer on the curvature of ultrathin 2D crystalline nanosheets and demonstrate that weak supramolecular forces within the organic part of colloidal nanocrystals can dramatically impact their shape. This transduction mechanism, in which changes in the organic monolayer impact the shape of a nanocrystal, will help devise new strategies to design stimuli-responsive systems that take advantage of both the flexibility of organic moieties and the physical properties of the inorganic core.

Keywords: Nanoplatelet — Nanoribbons — Polymorphism — Indium Sulfide — SAXS

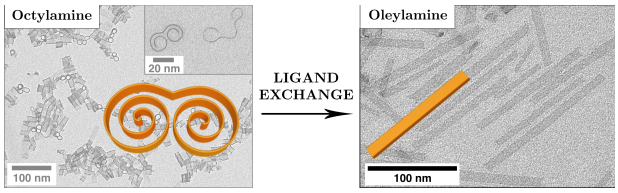

I. INTRODUCTION

The shape of inorganic nanoparticles is thought to be immutable. A range of post-synthesis transformations have been thoroughly studied in the past to change their composition [1], such as ion exchange [2] or the Kirkendall [3] effect. Still, once they have been synthesized, the crystalline structure can hardly be changed unless massive rearrangements occur through dissolution and recrystallization, generally under harsh chemical and temperature conditions. This contrasts with organic molecules or polymers in which the low energy barriers between different conformations allow for possible conversions *via* minor external stimuli or changes in their chemical environments such as temperature changes. Certain classes of nanocrystals, such as halide perovskites [4] or magic-sized clusters [5], are much more prone to post-synthesis transformations. For the former, this is due to their ionic bonds, which provide a high dynamic character to their crystalline lattice while, for the latter, their ultra-small size eases core reconfiguration [6]. Here, we show that ultrathin (with thickness in the nanometer range) nanoribbons (NR) can change their shape dramatically upon ligand exchange, even when the pre and post-exchange ligands bear the same attaching group. We trace this effect to ligand-induced surface stress, which depends on the structure of the ligand's alkyl chain.

The fact that adsorbates induce surface stresses on crystalline surfaces has been known for a long time[7, 8] and was first measured on thiol-capped gold cantilever[9]. Thiol molecules impose a compressive surface stress (in the 100 mN/m range) whose magnitude is directly proportional to the thiol alkyl chain length. In semiconducting nanomaterials, Meulenberg *et al.* showed that compressive or tensile surface stresses could be applied on quantum dots surface according to the electronic nature of the ligand (i.e. σ-donor or π-acceptor)[10].

In the case of 2D ultrathin nanoplatelets (NPL), these ligand-induced surface stresses can yield significant deformations [11]. So far, most of the examples in the literature concern cadmium chalcogenide nanoplatelets (NPL) [12], whose native surface ligands are exchanged for others bearing different functional groups. For instance, CdSe NPLs undergo a lateral deformation when native carboxylates are exchanged for aliphatic thiol or phosphonic acid, resulting in a shift up to 240 meV in the exciton transition [13]. Growing a CdS monolayer on tubular CdSe NPL unfolds them [14] while changes in ligand binding groups can lead to drastic changes in NPL shapes. For example, CdTe flat NPLs bend into nanotubes when carboxylates are exchanged for thiolates [15], leading to the formation of an extra CdS layer at the surface of the CdTe NPL. A tensile strain appears in

the CdS external layer, and a compressive strain in the CdTe core layer is present because of the mismatch in CdTe and CdS lattice parameters, resulting in conformation change. Dufour *et al.* [16] observed an unfolding of CdSe curved NPL when exchanging native carboxylates with halide ligands. This deformation is accompanied by an increase in the photoluminescence quantum yield of CdSe NPL up to 70 % along a redshift in their absorption features. These changes are interpreted by the variation in the NPL thickness due to an extension or contraction of the lattice induced by ligand exchange and a delocalization of the exciton wave function. Our group has also shown that large deformations in NPL shapes could be obtained without a change in the ligand functional group since CdSe flat NPL twist into helicoid upon the addition of oleic acid [17] in solution. More recently, the conformation of CdSe NPL was shown to depend on thiol ligand chain length [18, 19] and branching [20].

The concept of principal curvature is helpful to describe how NPL bend, curl, and adopt *in fine* their 3D shape. The two principal curvatures of a surface are the maximum and minimum values of the curvature at a given point along two orthogonal directions [21, 22]. The product of the two principal curvatures is the Gaussian curvature, whereas their average is the mean or Germain [23] curvature. These two quantities help define and classify the different canonical shapes (helicoid, tube, spiral) one can encounter with NPL [11, 20, 24]. Ligands at the surface of NPL induce a preferred curvature due to specific interactions between ligands and between ligands and the surface. These interactions can be encompassed in an effective curvature parameter whose value and the NPL's geometrical features dictate the NPL's geometry [20]. Due to the symmetry elements of the crystalline core, the ligand-induced curvatures at the top and bottom layers of the NPL can be orthogonal. This is the case for CdSe, whose zinc-blende crystal structure contains a $\bar{4}$ symmetry axis. An interplay between geometry and energy then dictates the shape of a thin NPL and can be accurately described using the incompatible theory framework [20], which has been used to describe macroscopic objects such as seed pods [25, 26] or surfactant self-assemblies [26, 27].

Beyond cadmium chalcogenides, few ultrathin NPLs have been shown to adopt various conformations. Though reports of Gd_2O_3 helices [28] or indium sulfide NR [29] prove that ultrathin 2D nanomaterials are ubiquitous, means to tune their conformations beyond changing the synthesis conditions are yet to be found. Indium sulfide is particularly relevant since it is often considered a non-toxic and more environmentally friendly alternative for heavy metals-based nanoparticles. For instance, In_2S_3 nanoparticles are used as buffer layers in photovoltaics[30] as well as in display devices and photodetectors[31–35] or for water splitting[36]. InS is envisaged for applications in photovoltaics too, as a potential passivation layer on InP devices[37, 38], as a compound combined with $CuInS_2$ for binary-based photovoltaic materials engineering[39], or for its *n*-type transport properties in thin films[40]. Spectroscopic properties are also reported for InS, such as Raman scattering[40, 41], photoluminescence[42, 43] and nonlinear optical properties[44]. Four InS allotropic varieties are referenced in the literature: orthorhombic, monoclinic, cubic, or tetragonal. Among them, the orthorhombic *Pnnm* InS structure is the most stable[45], with an optical band gap of 2.09 eV[44].

Here, we report the conformational control of initially coiled *n*-octylamine-capped ultrathin orthorhombic InS NR under the exchange of amino ligands. By increasing the length of the linear carbon chain of the primary amino ligand exchanged, we can tune the curvature of the NR. A complete uncoiling with a flat conformation is obtained with oleylamine. This fine control of the NR curvature is achieved by adjusting the carbon chain length of the surface ligand without any change in its anchoring group - always a primary amine - contrary to previous reports in the literature. Besides, this curvature control is demonstrated on a Cd-free material, paving the way for the conformation study, the supramolecular control, and the design of less toxic semiconducting nanomaterials.

II. RESULTS AND DISCUSSION

InS NR are synthesized from indium acetate and sulfur in *n*-octylamine by a solvothermal method inspired by Wang *et al.* [29, 46] (See experimental details in SI and Fig S1). After purification, Transmission Electron Microscopy (TEM) and high-angle annular dark field scanning TEM (HAADF-STEM) show NR with a thickness (e) of 0.90 ± 0.04 nm, a width (w) of 9 ± 2 nm and a length (L) of 138 ± 10 nm. In their native state, they display several different configurations (Fig. 1). The vast majority lie with their width perpendicular to the TEM grid and are significantly curved. The ribbons display an overall non-zero curvature along their length and a zero curvature along their width. They thus show a curvature typical of a tube with positive mean curvature and zero Gaussian curvature (Fig.1.a.-d.). However, the curvature along their length is not constant. If we start from an edge at one extremity of the ribbon and progress along the ribbon on a line parallel along its length (Fig. 1.e., 1.f.), the curvature decreases and cancels out at around half the length of the ribbons. After this midpoint, two configurations are observed. In some cases, the curvature becomes negative, but its absolute value increases (*in/out* configuration, Fig. 1.e.), while in other cases, the curvature increases again but remains positive. (*in/in* configuration, Fig 1.f.). The *in/out* configuration is chiral, while there is a plane of symmetry in the *in/in* configuration. To quantify the curvature of the NR from TEM images, we used an image treatment algorithm that allows the modeling of the curve from an initialization curve created manually by a point-click method which is then fitted to the underlying data using an iterative minimization al-

gorithm using cubic B-splines.

The average curvature is then calculated from the fitted curve (see Methods and Fig. S2). By repeating the measurement on a statistically relevant number of NR, we measure an average (5.6 ± 0.2) nm radius of curvature for *n*-octylamine-capped NR and an average length (L) of (138 ± 10) nm (Fig. 1.e. and 1.f.).

To determine the NR composition, we performed Rutherford Backscattering Spectrometry (RBS) (Fig. S3), which yields a ratio between indium and sulfur of (1.04 ± 0.04), leading to an InS empirical formula. The x-ray powder diffractogram (Fig. 3) displays three prominent broad peaks at 24.7°, 33.8°and 44.3°, eight others of low intensity, and two intense and narrow peaks at 27.2° and 29.2°. The widths of these peaks correspond to crystalline domains of 83 nm and 66 nm, i.e., much larger than all the NR dimensions, which points toward the presence of impurities. This is confirmed by XPS data, which indicate the presence of oxygen in the form of oxides (see Fig. S4). We deduce that impurities in the form of indium oxide are undoubtedly present in our sample, as suggested by the thin peaks at 21.3 °, 29.2 ° and 35.9 ° which are attributed to [211], [222] and [400] crystallographic planes of cubic indium sulfide In_2O_3 of the *Ia-3* space group (ICDD card n° 00-006-0416). Still, EDX mapping at the nanoscale shows that the NRs are only composed of indium and sulfur (Fig. 1.g.). Selected area electronic diffraction (SAED) confirms that the thin peaks in the X-ray diffraction are due to impurities since they do not appear in the SAED pattern (Fig. S5). The eight distances measured from SAED match the eight distances measured from XRD and are consistent with an orthorhombic *Pnnm* InS structure (ICDD card n° 01-072-0551, Fig. S5).

This crystallographic structure is confirmed by high-resolution STEM imaging, which proves the presence of a quaternary symmetry axis in the structure when the NRs are observed parallel or perpendicular to the thickness direction. Fourier transforms of STEM images (Fig. 2.c.-d.) match with electron diffraction of modeled orthorhombic InS along these directions(Fig. 2.e.-f.). The atomic disposition observed using HAADF-STEM is also consistent with the *Pnnm* structure. Rows of atoms oriented at approximately 45° from the edge are observed for a NR lying flat on the surface (Fig. 2.c.). When we observe the modeled NR lying on its edge (Fig. 2.d.), the atomic arrangements are consistent with these experimental observations: rows of 4 atoms or pairs of atoms that are oriented at approximately 40° from the edge. Besides, HR-STEM observations allow us to precisely determine the NR thickness of 0.90 ± 0.04 nm: this corresponds to the thickness of two *Pnnm* InS unit cells along the *b*-axis (0.88 nm, Fig. 2.f.).

We performed ligand exchange to explore the effect of surface ligands on the NR conformation (see SI for experimental details and Fig. S6). A significant excess of oleylamine coupled with the high reaction temperature ensures complete ligand exchange. TEM images of the purified product display completely uncoiled InS NR (Fig. 2.a.b.). To check that the high-temperature treatment did not cause the uncoiling, a control sample of InS NR in toluene (i.e., without adding oleylamine) was heated in the same experimental conditions. This control sample presented only coiled NR, similar to the ones observed before heating, with the same radius of curvature (5.6 ± 0.1) nm, confirming that the heating does not affect the conformation of the nano-object and just kinetically favors the ligand exchange. The uncoiling is thus due to the exchange of native *n*-octylamine with oleylamine, which changes the stress at the ligand/NR interface and induces their uncoiling.

To prove and quantify the extent of the exchange, thermogravimetric analyses (TGA) and Fourier-transform infrared (FT-IR) spectroscopy were performed on R-NH_2-capped (R = *n*-octyl or oleyl) InS NR. FT-IR spectroscopy shows for both samples characteristic stretching frequencies of the amine function (ν_{N-H}, 3000 - 3500 cm^{-1})[47]. In the case of the oleylamine-capped sample, an additional stretching band characteristic of the alkene vibration ($\nu_{=C-H}$, 3006 cm^{-1}) is observed. According to TGA results, initial *n*-octylamine-capped NR have a ligand density of 4.3 nm^{-2} (Fig. S9). After ligand exchange and assuming only one type of amine bound to the nanocrystal, we found an oleylamine ligand density of 3.1 nm^{-2} (Fig. S10.c.d.). 1D ^1H NMR and diffusion-ordered spectroscopy (DOSY) analyses were performed on oleylamine-capped sample (Fig. S11 and S12). The results support our assumption that oleylamine is effectively bound to nanocrystals. Indeed, two overlapping broad resonances are clearly visible in the alkene region (see insert in Fig. S12), characteristic of bound molecules. The same conclusion can be drawn from the DOSY experiment, which gives a lower diffusion coefficient for bound oleylamine (see SI section "*Surface characterization by NMR spectroscopy*").

To assess ligand-induced strain, we compare XRD patterns of coiled and uncoiled NR (Fig. 3). The two diffractograms display the same peaks corresponding to the *Pnnm* InS structure, but with their positions shifted (see Table I and red lines in Fig. 3). The strain δ_{coiled} applied along a specific [*hkl*] direction of coiled InS NR is defined as $\delta_{coiled} = (d_{coiled} - d_{bulk})/d_{bulk}$, with d_{coiled} the distance between two successive (*hkl*) atomic planes in the coiled NR crystallographic structure and d_{bulk} this distance in the bulk material.

Oleylamine and *n*-octylamine both exert compressive stresses in [101], [004], and [008] directions (negative strains values, see Table I) and a tensile stress in the [200] and [204] directions (positive strains values, see Table I). From a mechanical point of view, as the (200) plane is perpendicular to the (004) (or (008)) plane, tensile stress on the former has to engender compressive stress in the latter, hence the opposite sign of the strain imposed on these plans.

To better understand the role of the ligand alkyl chain in the uncoiling of the NR, we performed exchange exper-

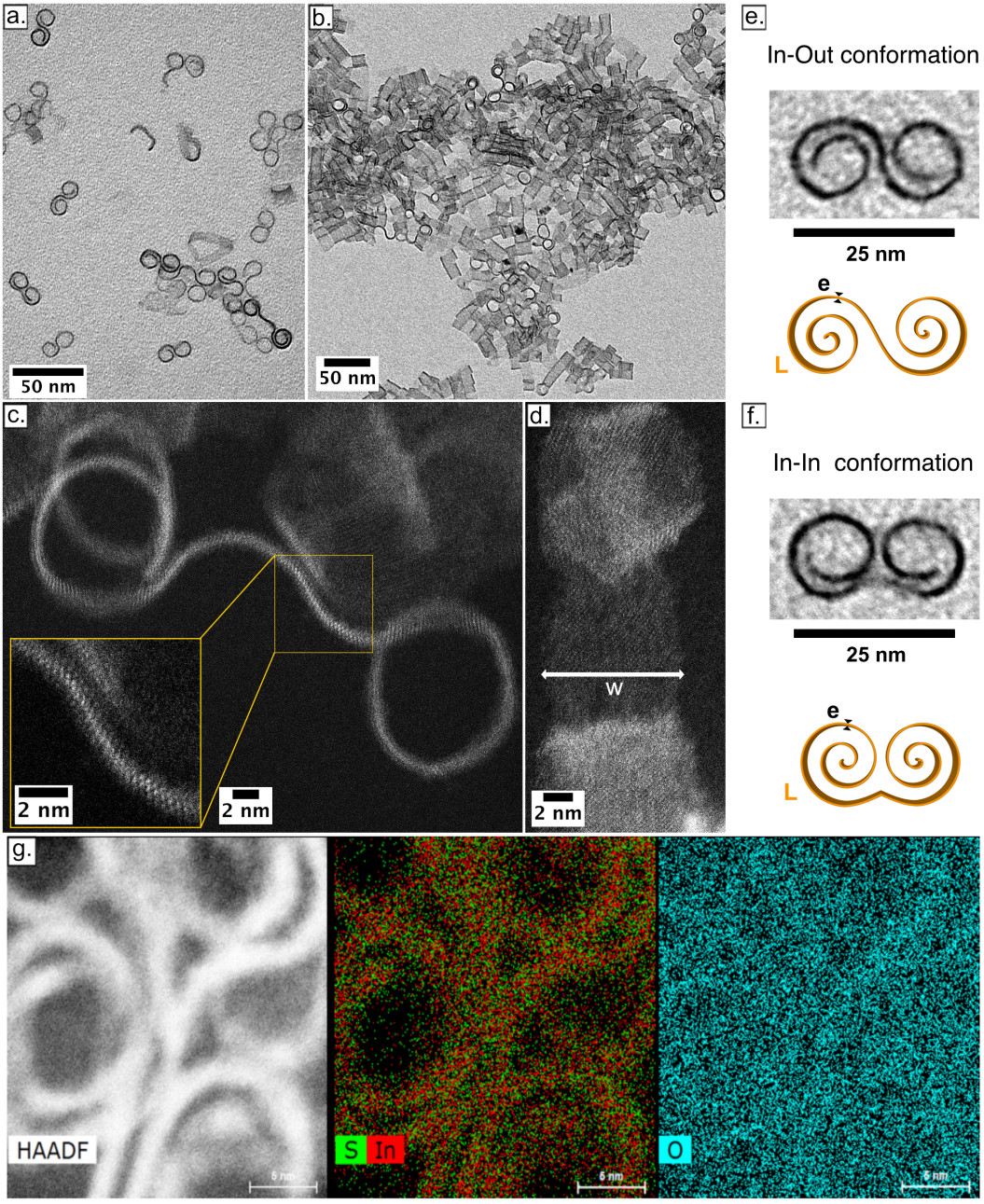

FIG. 1. TEM image of coiled InS NR lying edge-on (a.) and flat (b.) HR-STEM image of a coiled InS NR lying edge-on (c.) and flat (d.). Insert in (c.) is the enlargement of the yellow box – TEM images of InS NR in an *in/out* (e.) or an *in/in* (f.) conformation with their modeling according to Archimedean spirals (see SI for details). The notation w, e, and L correspond to the width (9 ± 2 nm), thickness (0.90 ± 0.4 nm), and length (138 ± 10 nm) measured by TEM, respectively. (g.) Elemental mapping of a coiled NR sample by Energy Dispersive X-ray spectroscopy (EDX). From left to right: HAADF-STEM image showing the area of the sample selected for EDX elemental mapping, indium and sulfur elemental mapping, and oxygen mapping.

iments with primary amines bearing different linear saturated alkyl chains with increasing ligand chain lengths from n-butylamine to n-octadecylamine. The experimental procedure is identical to the one described for oleylamine, which is described in the experimental section. The resulting NR were then characterized by TEM (Fig. 4, S7 and S8), from which the average curvature radii were measured as explained before (Fig.4.i.) and are compared with the ones of a control sample of octylamine (C8)-capped InS NR in toluene, heated 20 hours in a toluene solution of octylamine at 1.2M.

The nanoribbon's curvature is correlated to the length of the carbon chain of the amine ligand. A shorter carbon chain amine (i.e., n-butylamine (C4)) induces a

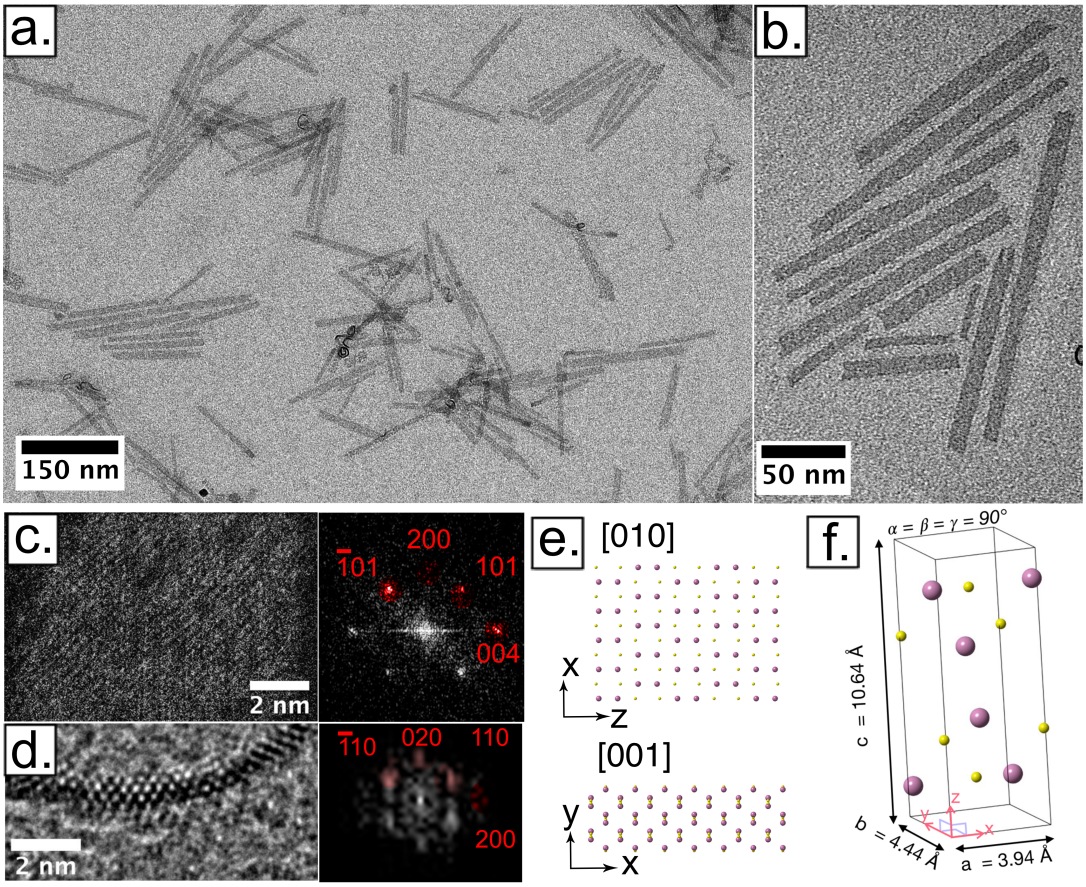

FIG. 2. (a-c.) TEM and HAADF-STEM images and their Fast Fourier Transform (FFT) of uncoiled InS NR lying flat at different magnifications. The indexation of the FFT spots corresponds to the InS orthorhombic structure. (d.) HAADF-STEM image of an uncoiled InS NR lying on its edge and its FFT. (e.) View of a modeled orthorhombic InS NR along the [010] and [001] zone axis. (f.) Scheme of an orthorhombic *Pnnm* InS conventional cell, from ICDD card n°01-072-0551.

Diffraction peak	[101]	[004]	[200]	[204]	[008]
2θ Bulk InS (°)	24.1	33.7	46.0	58.2	70.8
2θ(°) Coiled NR	24.7	33.8	44.3	56.4	70.9
2θ (°) Uncoiled NR	24.3	34.7	43.8	55.1	72.9
Strain (%) Coiled NR	-2.5	-0.4	3.7	3.0	-0.2
Strain (%) Uncoiled NR	-1.0	-3.0	4.8	5.2	-2.5

TABLE I. Shifts of diffraction peaks between coiled octylamine-capped NR and uncoiled oleylamine-capped NR and associated strains.

smaller curvature radius than in the control sample (i.e., with octylamine (C8), see Fig. 4) while octadecylamine (C18) leads to the highest InS NR radius of curvature radius measured. On the other hand, oleylamine, its non-saturated counterpart, leads systematically to a complete unfolding and flattening of the NR, i.e., infinite radius of curvature (Fig. 2, 4 and S8).

To further confirm the gradual uncoiling of the NR in solution with the ligand chain length, we performed Small-Angle X-ray Scattering (SAXS) measurements on these dispersions. This technique is adapted to get structural information on nanomaterials averaged over many nanoparticles and, more specifically, to assess the curvature of 2D nanoparticles [48–50]. Drying artifacts and interactions between the substrate and the nanoparticles, which can plague electron microscopy experiments, are also absent in SAXS since the measurement occurs in solution. SAXS patterns for the same nanoribbons coated with different alkylamine are shown in Fig. 4.j. At small wave vectors q, the intensity follows a q^{-2} power law consistent with the slenderness of the objects. At larger q, the intensity oscillates for the shorter chains (C4 to C14) while the q^{-2} scaling is conserved for the oleylamine case. For C16 and C18, the

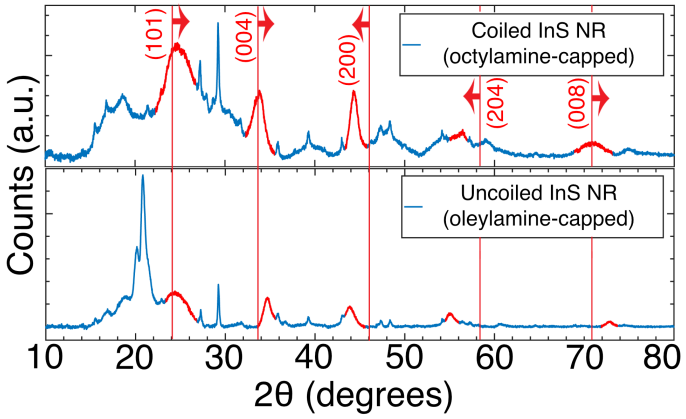

FIG. 3. X-Ray diffractograms of coiled octylamine-capped InS NR (top) and uncoiled oleylamine-capped InS NR (bottom). InS NR peaks that shift are highlighted in red. Peak shifting as regards bulk orthorhombic *Pnnm* InS (ICDD card n° 01-072-0551) diffraction peak positions are highlighted by red lines and arrows.

oscillations are much less marked than for the shorter chains. The oscillations appear at q values between 0.05 and 0.1 Å^{-1}, corresponding to distances between 6 and 12 nm in real space. As already shown for CdSe NPL [14], they are fingerprints of the curvature of nanoplates with a typical radius of curvature on this length scale. More details of these features can be seen in the Kratky plot (Iq^2 vs q) in Fig. 4.k. We note that for each sample, oscillation positions shift depending on the ligand chain length. Hence, we can classify our samples into three categories depending on their SAXS patterns. For n-butylamine (C4)-, n-hexylamine (C6)- and n-octylamine (C8)-capped samples, the maximum of the oscillations appears between 0.6 and 0.8 Å^{-1} while they shift at smaller q for C12 and C14. The oscillations get weaker for n-hexadecylamine (C16)- and n-octadecylamine (C18)-capped samples and disappear for oleylamine (OLAM)-capped sample, which displays a constant Kratky plot indicating a flat object with an infinite radius of curvature. Hence, the SAXS patterns are consistent with gradually uncoiling the ribbons as the ligand chain length increases. To go beyond this qualitative picture, we simulated SAXS patterns of Archimedean spirals, which are idealized shapes of the InS NR (see SI for details). The theoretical SAXS patterns share common features with the experimental ones, such as a q^{-2} regime at small angles and a large oscillation whose position depends on the curvature. We find a direct relation between the Kratky plot's oscillation maximum and the NR's curvature radius (Fig. S15). By applying this model to our experimental data, we extract a radius of curvature by SAXS between 5 and 7.5 nm for chain lengths between 4 and 8 in quantitative agreement with TEM. We note, however, that the increase in curvature radius between C4 and C8 observed by TEM is not visible in the SAXS data. For C14 and C16, the oscillation position is more difficult to assess with certainty since the patterns are noisier and featureless. It is also likely that the Archimedean spiral model does not describe the shape of the ribbon due to its larger uncoiling. Overall, these SAXS experiments and their modeling give a direct insight into the conformation of the NR in solution, which is in semi-quantitative agreement with TEM.

We now examine the possible physical origin of this trend in the framework of incompatible elasticity theory, which is relevant for ribbons covered with a monolayer of surfactants [20]. We showed that ribbons display an effective curvature given by:

$$\bar{\kappa} = \Psi \kappa_0 \frac{\Phi^3}{1+\Phi^3}, \tag{1}$$

where κ_0 is the curvature at the NPL/ligand interface, $\Psi = Y_{\text{lig}}/Y_{\text{bulk}}$ is the ratio between the interfacial and bulk Young's moduli, and $\Phi = e/t$ is the ratio between the effective thickness of the surfactant layer and the NPL thickness. Here, we observe a decrease in the ribbon's curvature as the ligand chain length increases for linear alkyl chains. A similar trend was observed previously for CdSe in experiments [19] and simulation [20]. This physical parameter impacts all the terms in equation 1 directly or indirectly. First, it appears through the $\frac{\Phi^3}{1+\Phi^3}$ term *via* the thickness of the surfactant monolayer e. However, this term increases with e at constant ribbon thickness. Hence, if it predominated, we would observe an increasing curvature with increasing ligand's chain length and not a decrease as we do. The ligand chain length also impacts Ψ *via* Y_{lig}. The bending rigidity of a monolayer is known to increase with the surfactant tail length [51]. Here again, the dependence does not correspond to our experimental findings but the ligand tail length can also play a role in variations of κ_0. The spontaneous curvature of a monolayer results from an interplay between the repulsion of the headgroup and the attraction between the chains. The so-called packing parameter p is often used for surfactants at air/water and water/oil interfaces to get insight on the preferred curvature adopted by monolayers [52]: $p = \frac{v}{a_0 \ell_c}$, where v is the volume occupied by the surfactant tail, a_0 is the area per surfactant head and ℓ_c the length of the alkyl length. The ratio $\frac{v}{\ell_c}$ is almost constant with chain length for linear alkyl chains [53] while the area per ligand depends mostly on the headgroup. In our case, it is reasonable to assume that this parameter is constant over amine ligand exchange but Anderson *et al.* recently shown that surface ligand surface densities depend strongly on the ligand structure beyond their polar heads [54]. Thus, the ligand chain length could impact the packing parameter through variations of surface densities over ligand exchange. The dramatic change in curvature observed between oleyl and octadecyl chains could also be explained by such differences in ligand surface density. Furthermore, unsaturation has been shown to decrease

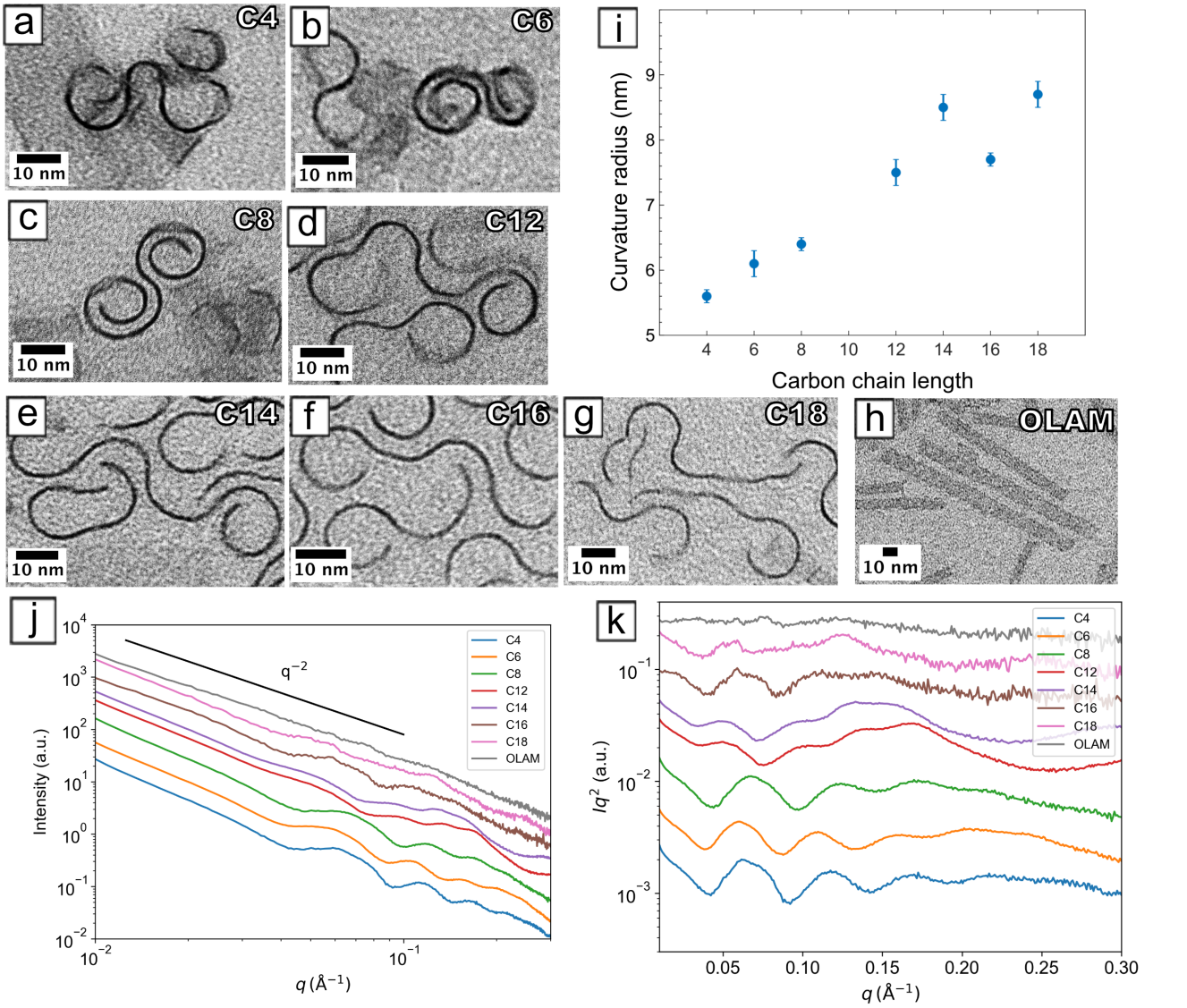

FIG. 4. Effect of amine chain length on NR curvature (a-h.) TEM images of InS NR capped with *n*-butylamine (C4), *n*-hexylamine (C6), *n*-octylamine (C8), *n*-dodecylamine (C12), *n*-tetradecylamine (C14), *n*-hexadecylamine (C16), *n*-octadecylamine (C18), and oleylamine (OLAM) showing the gradual uncoiling of the NR with the increase in the carbon chain length of the amine ligand. (i.) Mean radius of curvature as a function of the carbon chain length between *n*-butylamine and *n*-octadecylamine as measured by TEM. (j.) SAXS pattern and (k.) Kratky plot (Iq^2 vs q) of the SAXS intensity for the same InS nanoribbons with different *n*-alkylamines.

lipid bilayers' bending modulus significantly. Hence, going from octadecyl to oleyl chain would induce a decrease in Ψ and thus a decrease in curvature in line with experiments. More efforts towards a molecular description of the nanocrystal/ligand interface are needed to disentangle these different effects and quantify them.

III. CONCLUSION

We have shown that control of the coiling of InS NR is easily achieved by choosing an appropriate surface ligand. Ligand exchanges were realized between native *n*-octylamine and primary amines, which differ only in their saturated linear carbon chain length. TEM radius curvature measurements and SAXS allow monitoring of the NR's conformation depending on the amine chain length. Short carbon chains lead to the highest curvatures, and oleylamine entirely unfolds the initially coiled NR. While the folding or unfolding of NPL has been achieved up to now through the grafting of different functional groups at their surface, our work shows that curvature control can be achieved by choosing the ligand chain length and saturation. This demonstrates that alkyl chain interactions within the ligand monolayer play a significant role in surface stress, which controls NPL conformation. The fact

that the shape of ultrathin nanoparticles can be tuned to such an extent by low energy interactions at their surface paves the way toward supramolecular control of nanoparticle conformation.

ACKNOWLEDGMENTS

This article is part of a project that has received funding from the European Research Council (ERC CoG SENECA) under the European Union's Horizon 2020 research and innovation program (Grant Agreement No. 865995). This work was supported by the LABEX iMUST of the University of Lyon (ANR-10-LABX-0064), created within the program "Investissements d'Avenir" set up by the French government and managed by the French National Research Agency (ANR). We acknowledge CIQLE for providing transmission electron microscopy facilities, especially Bruno Chapuis and Elisabeth Errazuriz. The authors thank Frédéric Chaput for his precious help and expertise in synthesizing materials by solvothermal route, Marta de Frutos for discussions about HR-STEM and Frédéric Lerouge for help during the TGA measurements. SERMA technologies are acknowledged for XPS measurements. RBS analyses were performed with the help of Bruno Canut from the INL.

MATERIALS AND METHODS

IV. EXPERIMENTAL METHODS

A. Starting Materials and chemicals

Indium (III) acetate (anhydrous, 99.9%), *n*-octylamine (99+%), and oleylamine (approximate C18-content 80-90%) were purchased from Fisher-Acros Organics. Sulfur (powder, 99.998%), *n*-hexadecylamine (98%), and *n*-dodecylamine (98%) were purchased from Sigma-Aldrich. *n*-Tetradecylamine (≥96%) was purchased from TCI Europe. *n*-Butylamine (99%) and *n*-octadecylamine (97%) were purchased from Fisher-Alfa Aesar. Absolute ethanol and toluene (∼99.5%) were purchased from VWR.

B. Instrumentation

Transmission Electron microscopy (TEM). TEM images were acquired on a JEOL JEM-1400 (accelerating voltage of 120 kV) at CIQLE Lyon. The samples are prepared by drop-casting InS NR suspensions in toluene onto 200 carbon-coated copper grids. To avoid aggregation of NR on the TEM grids, the suspension of NR can be diluted to minima by a factor of ten and sonicated for 2 minutes in a bath. InS ultra-thin NR are electron beam sensitive and may deteriorate in a few seconds. Part of HR-STEM pictures have been acquired using a Jeol Neoarm operating at 200 kV at the Centre Électronique de Microscopie Stéphanois, in Saint-Étienne (France). STEM observations were made on a Titan Themis 200 microscope (FEI/ Thermo Fischer Scientific) equipped with a geometric aberration corrector on the probe at the center of nanosciences and nanotechnologies of Palaiseau. The microscope was also equipped with the "Super-X" systems for EDX analysis with a detection angle of 0.9 steradian. The observations were made at 200 kV with a probe current of about 50 pA and a half-angle of convergence of 17 mrad. HAADF-STEM images were acquired with a camera length of 110 mm (inner/outer collection angles were 69 and 200 mm, respectively). The HRTEM images and selected area electron diffraction patterns (SAED) were acquired on a Ceta 16M camera. The camera length for the electron diffraction was 100 cm with a spot size of 5 to minimize the irradiation of the sample.

Powder X-Ray Diffraction (XRD). XRD data were acquired using a PANalytical Empyrean X-ray diffractometer equipped with a 1.8 kW Cu Kα ceramic tube, operating at 45 kV and 40 mA and a PIXcel3D 2×2 area detector.

Small Angle X-ray Scattering (SAXS). SAXS experiments were performed on a Xenocs XEUSS 3.0 apparatus using an X-ray energy of 8 keV with a sample-to-detector distance of 350 mm. InS NR dispersions were loaded in glass capillaries.

Rutherford backscattering spectrometry (RBS).. RBS was used to measure the mean atomic composition [S]/[In]. For this purpose, the sample, initially in powder form, was deposited on carbon adhesive tape. The analysis was performed with $4He^+$ ions of 2 MeV energy delivered by the 4 MV Van de Graaff accelerator of the "ANAFIRE" platform located at the Institut de Physique des 2 Infinis (IP2I) Laboratory of Lyon. The backscattered particles were detected with a 15 keV resolution implanted junction set at an angle of 169° with respect to the beam axis. The experimental data were fitted with the help of the SIMNRA simulation code [55].

X-ray Photoelectron Spectroscopy (XPS). XPS spectra were recorded on a THERMO K-alpha+ spectrometer with the Al Kα line used as the excitation source at the Laboratoire Science et Surface of Ecully (Serma Technologies).

Fourier-Transform Infrared Spectroscopy (FT-IR). FT-IR analyses were carried out on Perkin-Elmer Spectrum 65 spectrometer in transmission mode and using Specac Omnicell equipped with two KBr windows. Samples were dispersed in tetrachloroethylene to perform the solution-phase measurements.

Nuclear Magnetic Resonance (NMR). NMR analyses were carried out on Bruker Advanced 400MHz spectrometer equipped with a 5 mm Prodigy probe. ^{1}H spectra were calibrated using TMS standard and chemical shift values are provided in ppm. Deuterated solvents were dried over CaH_2 and distilled.

C. Solvothermal synthesis of indium sulfide NR

0.0511 g of anhydrous indium (III) acetate (0.175 mmol, 1 eq.), 0.0056 g of sulfur powder (0.175 mmol, 1 eq.), 12.25 mL of 1-*n*-octylamine and 1.75 mL of absolute ethanol are introduced in a 20 mL Teflon-lined autoclave. The reaction mixture is ultrasonicated for 10 minutes to get a homogeneous solution. The autoclave is sealed and heated at 220°C for 12h in an oven. Once it is cooled to room temperature, the yellow-cloudy resulting solution is centrifuged for 5 minutes at 6153×g. The product is redispersed in 5 mL of absolute ethanol before being centrifuged for 5 minutes at 6153×g. This procedure is reproduced twice in a mixture of 5 mL of toluene and 3 mL of ethanol and twice in 5 mL of toluene. The final yellow product is redispersed in 20 mL of toluene. The typical mass concentration at this stage is 1.3 g/L.

D. Unfolding of indium sulfide NR by ligand exchange

A typical procedure to unfold completely as-synthesized *n*-octylamine-capped InS nanoribbons is to add 355 μL of oleylamine (final concentration in solution of 1.2 M) to 150 μL of the above solution of folded NR (final concentration in solution of 0.22 mg/mL) and 395 μL of toluene in a vial. The mixture is then sonicated for 10 minutes before being heated for 21h under agitation (150 rpm) at 95°C in an oil bath. 500 μL of absolute ethanol is added, and the mixture is centrifuged for 5 minutes at 6153×g: the residue of unfoldedInS NR is then redispersed in 1 mL of toluene. This last step can be repeated twice to get rid of oleylamine traces.

The same procedure above is then applied, using different amino ligands instead of oleylamine (used for complete unfolding): *n*-butylamine (maximal coiling), *n*-dodecylamine, *n*-tetradecylamine, *n*-hexadecylamine, *n*-octadecylamine (unfolding) with a 1.2 M final amino ligand concentration in the solution. Oleylamine-capped InS nanoribbon samples are colloidally stable, contrary to other amine-capped InS nanoribbon samples, which precipitate within a few hours.

E. TEM curvature measurements

To quantify the coiling inside a sample, we use a semi-automatic image treatment algorithm (ImageJ plugin Kappa, `https://github.com/fiji/Kappa`) [56] which detects the contour of the NR, measures the curvature along its length and computes the mean curvature and thus the average curvature radius of the NR. The Fiji plugin Kappa allows modeling the curve adopted by an NR viewed along its side on TEM images from an initialization curve created manually by a point-click method (see Figure S2). The initialization curve is then fit by the software to the underlying data using an iterative minimization algorithm that uses cubic B-splines (i.e., parametric piecewise 3rd-degree Bézier curves Considering one NR and for each point on the line is then calculated the curve length, the curvature κ and so the radius of curvature ρ which is defined as the inverse of κ. This radius of curvature is then averaged for the whole modeled NR. By repeating this procedure to a hundred NRs of the sample, we can give an averaged and global radius of curvature of the NR inside the sample. The associated uncertainty U of this global curvature (or of the radius of curvature) is calculated as follows: $U = 2\sigma/\sqrt{n}$ with σ the square deviation of the statistical series and n the number of measurements (i.e., the number of NR of the sample for which we measure the curvature, about a hundred). As regards uncertainties, we consider only A-type uncertainty for curvature measurements, as B-type uncertainties are evaluated as much smaller than A-type uncertainty (This is not the case for the measurement of the dimensions of flat NR, where A-type uncertainty U_A and B-type uncertainties U_B have both to be taken into account).

[1] L. Manna, J. Cheon, and R. E. Schaak, Why Do We Care about Studying Transformations in Inorganic Nanocrystals?, Accounts of Chemical Research **54**, 1543 (2021).

[2] L. De Trizio and L. Manna, Forging Colloidal Nanostructures via Cation Exchange Reactions, Chemical Reviews **116**, 10852 (2016).

[3] Y. Yin, R. M. Rioux, C. K. Erdonmez, S. Hughes, G. A. Somorjai, and A. P. Alivisatos, Formation of Hollow Nanocrystals Through the Nanoscale Kirkendall Effect, Science **304**, 711 (2004).

[4] N. Pradhan, Alkylammonium Halides for Facet Reconstruction and Shape Modulation in Lead Halide Perovskite Nanocrystals, Accounts of Chemical Research **54**, 1200 (2021).

[5] C. B. Williamson, D. R. Nevers, A. Nelson, I. Hadar, U. Banin, T. Hanrath, and R. D. Robinson, Chemically reversible isomerization of inorganic clusters, Science **363**, 731 (2019).

[6] H. Han, Y. Yao, and R. D. Robinson, Interplay between Chemical Transformations and Atomic Structure

in Nanocrystals and Nanoclusters, Accounts of Chemical Research **54**, 509 (2021).
[7] H. Ibach, Adsorbate-induced surface stress, J. Vac. Sci. Technol. A **12**, 2240 (1994).
[8] R. C. Cammarata, Surface and interface stress effects in thin films, Prog. Surf. Sci. **46**, 1 (1994).
[9] R. Berger, E. Delamarche, H. P. Lang, C. Gerber, J. K. Gimzewski, E. Meyer, and H.-J. Güntherodt, Surface stress in the self-assembly of alkanethiols on gold, Science **276**, 2021 (1997).
[10] R. W. Meulenberg, T. Jennings, and G. F. Strouse, Compressive and tensile stress in colloidal CdSe semiconductor quantum dots, Phys. Rev. B **70**, 235311 (2004).
[11] L. Guillemeney, L. Lermusiaux, G. Landaburu, B. Wagnon, and B. Abécassis, Curvature and self-assembly of semi-conducting nanoplatelets, Commun. Chem. **5**, 1 (2022).
[12] S. Ithurria, M. D. Tessier, B. Mahler, R. P. S. M. Lobo, B. Dubertret, and A. L. Efros, Colloidal nanoplatelets with two-dimensional electronic structure, Nat. Mater. **10**, 936 (2011).
[13] A. Antanovich, A. W. Achtstein, A. Matsukovich, A. Prudnikau, P. Bhaskar, V. Gurin, M. Molinari, and M. Artemyev, A strain-induced exciton transition energy shift in CdSe nanoplatelets: The impact of an organic ligand shell, Nanoscale **9**, 18042 (2017).
[14] C. Bouet, B. Mahler, B. Nadal, B. Abécassis, M. D. Tessier, S. Ithurria, X. Xu, and B. Dubertret, Two-dimensional growth of CdSe nanocrystals, from nanoplatelets to nanosheets, Chem. Mater. **25**, 639 (2013).
[15] R. B. Vasiliev, E. P. Lazareva, D. A. Karlova, A. V. Garshev, Y. Yao, T. Kuroda, A. M. Gaskov, and K. Sakoda, Spontaneous folding of CdTe nanosheets induced by ligand exchange, Chem. Mater. **30**, 1710 (2018).
[16] M. Dufour, J. Qu, C. Greboval, C. Méthivier, E. Lhuillier, and S. Ithurria, Halide ligands to release strain in cadmium chalcogenide nanoplatelets and achieve high brightness, ACS Nano **13**, 5326 (2019).
[17] S. Jana, M. de Frutos, P. Davidson, and B. Abécassis, Ligand-induced twisting of nanoplatelets and their self-assembly into chiral ribbons, Sci. Adv. **3**, e1701483 (2017).
[18] Q. Martinet, J. Baronnier, A. Girard, T. Albaret, L. Saviot, A. Mermet, B. Abecassis, J. Margueritat, and B. Mahler, Ligand-dependent nano-mechanical properties of CdSe nanoplatelets: calibrating nanobalances for ligand affinity monitoring, Nanoscale **13**, 8639 (2021).
[19] H. Po, C. Dabard, B. Roman, E. Reyssat, J. Bico, B. Baptiste, E. Lhuillier, and S. Ithurria, Chiral helices formation by self-assembled molecules on semiconductor flexible substrates, ACS Nano **16**, 2901 (2022).
[20] D. Monego, S. Dutta, D. Grossman, M. Krapez, P. Bauer, A. Hubley, J. Margueritat, B. Mahler, A. Widmer-Cooper, and B. Abécassis, Ligand-induced incompatible curvatures control ultrathin nanoplatelet polymorphism and chirality, Proceedings of the National Academy of Sciences **121**, e2316299121 (2024).
[21] S. Hyde, Z. Blum, T. Landh, S. Lidin, B. W. Ninham, S. Andersson, and K. Larsson, *The language of shape – The role of curvature in condensed matter: Physics, chemistry and biology* (Elsevier B. V., Amsterdam, 1997).
[22] R. D. Kamien, The geometry of soft materials: A primer, Rev. Mod. Phys. **74**, 953 (2002).
[23] D. P. Holmes, Germain curvature: The case for naming the mean curvature of a surface after sophie germain, arXiv preprint arXiv:2303.13615 (2023).
[24] R. Ghafouri and R. Bruinsma, Helicoid to spiral ribbon transition, Phys. Rev. Lett. **94**, 138101 (2005).
[25] S. Armon, E. Efrati, R. Kupferman, and E. Sharon, Geometry and mechanics in the opening of chiral seed pods, Science **333**, 1726 (2011).
[26] S. Armon, H. Aharoni, M. Moshe, and E. Sharon, Shape selection in chiral ribbons: From seed pods to supramolecular assemblies, Soft Matter **10**, 2733 (2014).
[27] M. Zhang, D. Grossman, D. Danino, and E. Sharon, Shape and fluctuations of frustrated self-assembled nano ribbons, Nat. Commun. **10**, 3565 (2019).
[28] Y. Liu, Y. Li, S. Jeong, Y. Wang, J. Chen, and X. Ye, Colloidal synthesis of nanohelices via bilayer lattice misfit, J. Am. Chem. Soc. **142**, 12777 (2020).
[29] P. peng Wang, Y. Yang, J. Zhuang, and X. Wang, Self-adjustable crystalline inorganic nanocoils, J. Am. Chem. Soc. **135**, 6834 (2013).
[30] E. Dalas, S. Sakkopoulos, E. Vitoratos, G. Maroulis, and L. Kobotiatis, Aqueous precipitation and electrical properties of In_2S_3: Characterization of the In_2S_3/polyaniline and In_2S_3/polypyrrole heterojunctions, J. Mater. Sci. **28**, 5456 (1993).
[31] K. H. Park, K. Jang, and S. U. Son, Synthesis, optical properties, and self-assembly of ultrathin hexagonal In_2S_3 nanoplates, Angew. Chem. Int. Ed. **45**, 4608 (2006).
[32] S.-H. Choe, T.-H. Bang, N.-O. Kim, H.-G. Kim, C.-I. Lee, M.-S. Jin, S.-K. Oh, and W.-T. Kim, Optical properties of β-In_2S_3 and β-In_2S_3:Co^{2+} single crystals, Semicond. Sci. Technol. **16**, 98 (2001).
[33] S. Gorai, P. Guha, D. Ganguli, and S. Chaudhuri, Chemical synthesis of β-In_2S_3 powder and its optical characterization, Mater. Chem. Phys. **82**, 974 (2003).
[34] J. Tang, G. Konstantatos, S. Hinds, S. Myrskog, A. G. Pattantyus-Abraham, J. Clifford, and E. H. Sargent, Heavy-metal-free solution-processed nanoparticle-based photodetectors: Doping of intrinsic vacancies enables engineering of sensitivity and speed, ACS Nano **3**, 331 (2009).
[35] S. Acharya, M. Dutta, S. Sarkar, D. Basak, S. Chakraborty, and N. Pradhan, Synthesis of micrometer length indium sulfide nanosheets and study of their dopant induced photoresponse properties, Chem. Mater. **24**, 1779 (2012).
[36] M. Li, X. Tu, Y. Su, J. Lu, J. Hu, B. Cai, Z. Zhou, Z. Yang, and Y. Zhang, Controlled growth of vertically aligned ultrathin In_2S_3 nanosheet arrays for photoelectrochemical water splitting, Nanoscale **10**, 1153 (2018).
[37] A. N. MacInnes, M. B. Power, A. F. Hepp, and A. R. Barron, Indium tert-butylthiolates as single source precursors for indium sulfide thin films: Is molecular design enough?, J. Organomet. Chem. **449**, 95 (1993).
[38] R. Iyer, R. R. Chang, and D. L. Lile, Sulfur as a surface passivation for InP, Appl. Phys. Lett. **53**, 134 (1988).
[39] R. Kumaresan, M. Ichimura, N. Sato, and P. Ramasamy, Application of novel photochemical deposition technique for the deposition of indium sulfide, Mater. Sci. Eng. B **96**, 37 (2002).

[40] C.-L. Tu, K.-I. Lin, J. Pu, T.-F. Chung, C.-N. Hsiao, A.-C. Huang, J.-R. Yang, T. Takenobu, and C.-H. Chen, CVD growth of large-area InS atomic layers and device applications, Nanoscale **12**, 9366 (2020).

[41] N. M. Gasanly, H. Özkan, A. Aydinli, and I. Yilmaz, Temperature dependence of the Raman-active phonon frequencies in indium sulfide, Solid State Commun. **110**, 231 (1999).

[42] N. M. Gasanly and A. Aydinli, Low-temperature photoluminescence spectra of InS single crystals, Solid State Commun. **101**, 797 (1997).

[43] A. Othonos and M. Zervos, Carrier dynamics in InS nanowires grown via chemical vapor deposition, Phys. Status Solidi A **207**, 2258 (2010).

[44] P. Kushwaha, A. Patra, E. Anjali, H. Surdi, A. Singh, C. Gurada, S. Ramakrishnan, S. Prabhu, A. Venu Gopal, and A. Thamizhavel, Physical, optical and nonlinear properties of InS single crystal, Opt. Mater. **36**, 616 (2014).

[45] H.-Y. Wang, X.-F. Li, L. Xu, X.-S. Li, and Q.-K. Hu, Phase transition and physical properties of InS, Commun. Theor. Phys. **69**, 211 (2018).

[46] B. Ni, H. Liu, P.-p. Wang, J. He, and X. Wang, General synthesis of inorganic single-walled nanotubes, Nat. Commun. **6**, 8756 (2015).

[47] K. C. Dümbgen, I. Infante, and Z. Hens, Localizing Oleylamine Ligands on Amine–Halide Copassivated Indium Phosphide Nanocrystals, Chemistry of Materials **35**, 4393 (2023), publisher: American Chemical Society.

[48] N. Castro, C. Bouet, S. Ithurria, N. Lequeux, D. Constantin, P. Levitz, D. Pontoni, and B. Abécassis, Insights into the formation mechanism of CdSe nanoplatelets using in situ x-ray scattering, Nano Lett. **19**, 6466 (2019).

[49] J. Maes, N. Castro, K. D. Nolf, W. Walravens, B. Abécassis, and Z. Hens, Size and concentration determination of colloidal nanocrystals by small-angle X-ray scattering, Chem. Mater. **30**, 3952 (2018).

[50] D. Constantin, Solution scattering from colloidal curved plates: Barrel tiles, scrolls and spherical patches, Journal of Applied Crystallography **48**, 1901 (2015).

[51] A. Würger, Bending Elasticity of Surfactant Films: The Role of the Hydrophobic Tails, Physical Review Letters **85**, 337 (2000).

[52] J. N. Israelachvili, *Intermolecular and Surface Forces* (Academic Press, 2010).

[53] C. Tanford, Micelle shape and size, The Journal of Physical Chemistry **76**, 3020 (1972).

[54] N. C. Anderson, Peter. E. Chen, A. K. Buckley, J. De Roo, and J. S. Owen, Stereoelectronic Effects on the Binding of Neutral Lewis Bases to CdSe Nanocrystals, Journal of the American Chemical Society 10.1021/jacs.8b02927 (2018).

[55] M. Mayer, Simnra user's guide ipp 9/113 max-planck-institut fur plasmaphysik, Garching, Germany (1997).

[56] H. Mary and G. J. Brouhard, Kappa (κ): Analysis of Curvature in Biological Image Data using B-splines (2019)

SUPPLEMENTARY MATERIAL

A. Supplementary Figures

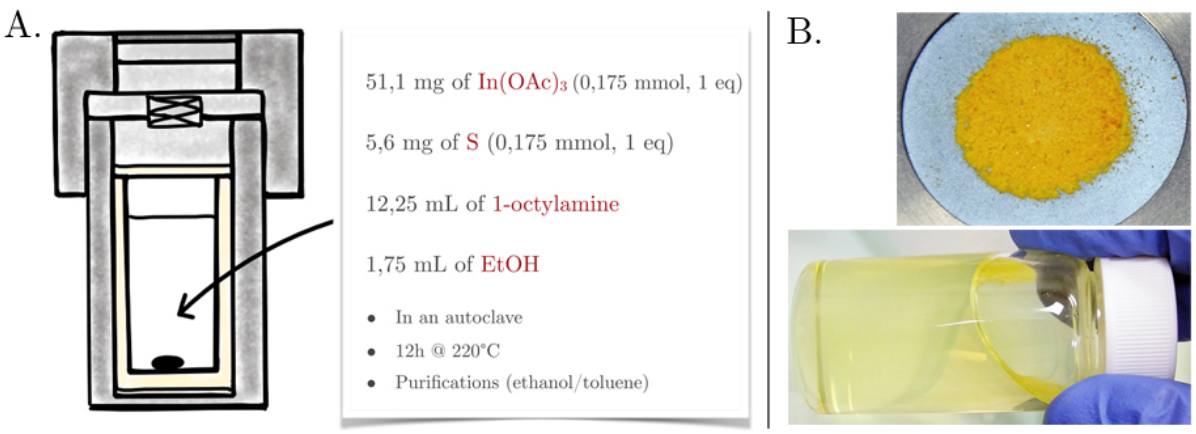

FIG. S1. A. Scheme of the experimental conditions - B. Top: Nanoribbons in the powder form, Bottom: Colloidal solution of nanoribbons dispersed in toluene.

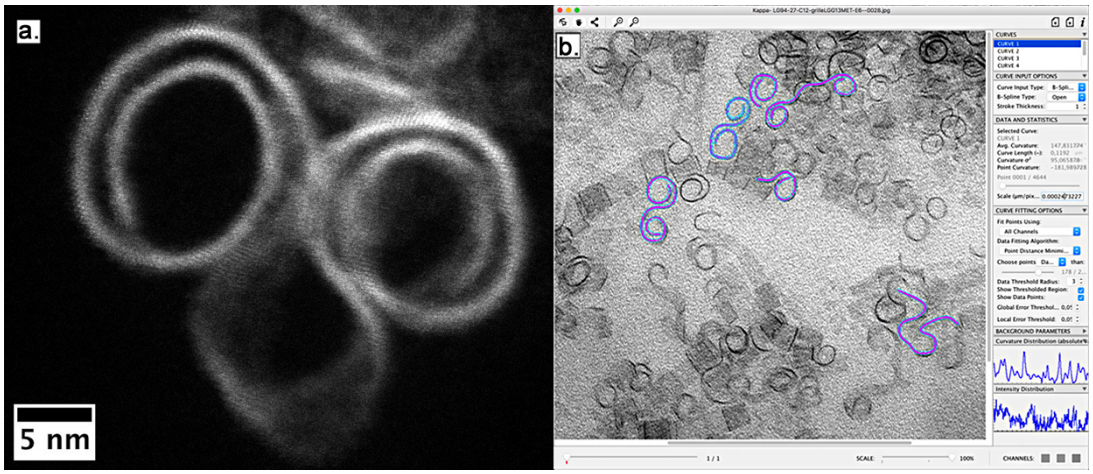

FIG. S2. (a.) HAADF-STEM images of *n*-octylamine-capped coiled InS NR lying on edge, highlighting these nano-objects high degree of curvature. - (b.) Screenshot of Kappa plugin interface: in purple is represented the fit curve obtained from an initialization curve created by a point-click method, which follow the observed curve of the NR.

B. Thermogravimetric analysis (TGA) and FT-IR experiments

TG analyses on amine-capped InS NR are used to calculate the surface ligand density of amines. From the mass fraction of ligands obtained using TGA, the surface coverage is expressed through equation 1:

$$\omega_l = \frac{1}{1 + \frac{X}{\Sigma}} \tag{2}$$

where $X = \frac{\mathcal{N}_A V_{NR} \rho_{NR}}{\mathcal{A}_{NR} M_l}$, $\mathcal{N}_A$ is the Avogadro constant, $\mathcal{A}_{NR}$, V_{NR} and ρ_{NR} are the surface area, the volume and the density (4.92 g.cm^{-3}) of the InS NR, respectively. M_l is the molecular weight of the ligand considered. We found

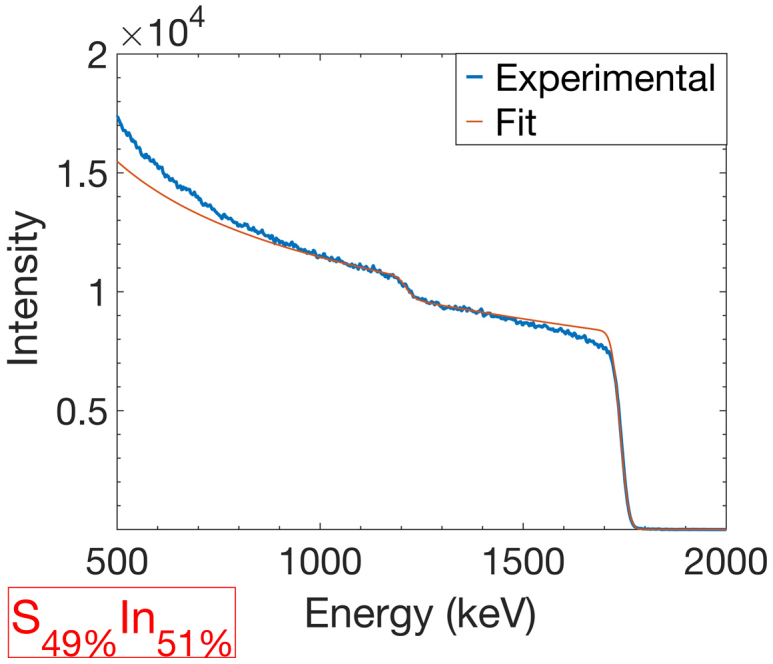

FIG. S3. RBS spectrum for NR: the experimental data are fitted in order to obtain the chemical composition of the sample, written below the spectrum.

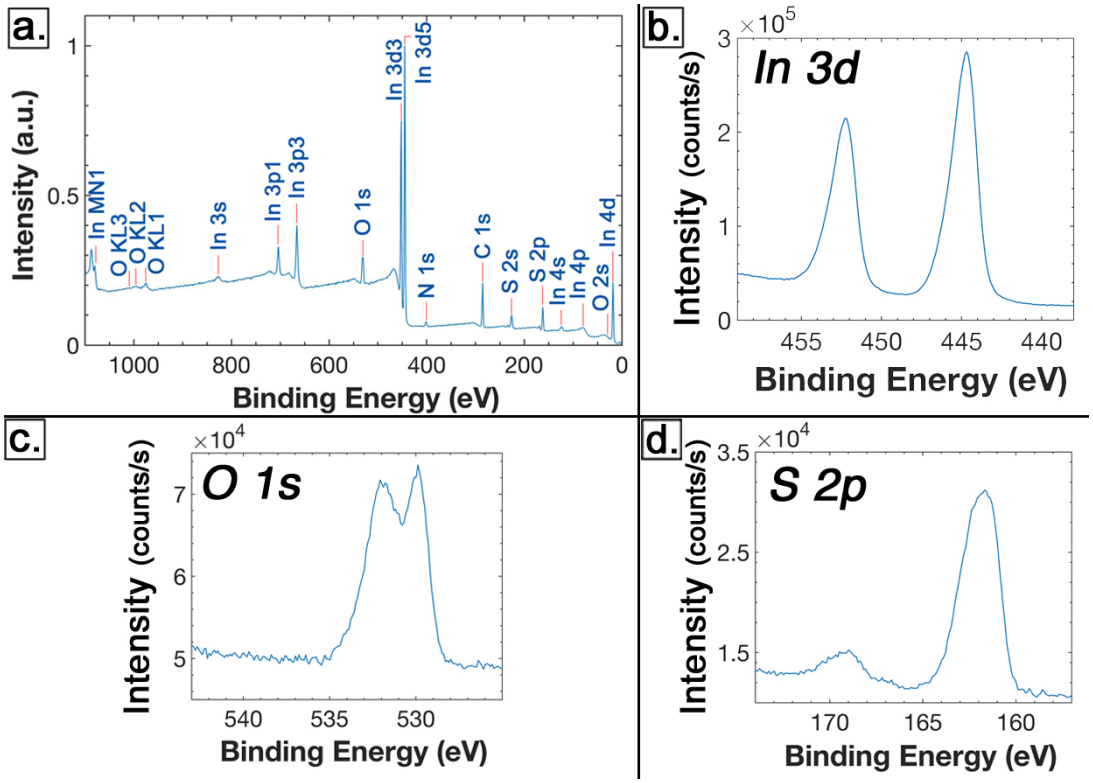

FIG. S4. XPS analyses: (a.) XPS survey patterns InS nanoribbons, proving the atomic presence of In(16.3%), S(14.7%), O(18.9%), C(45.3%), N(4.8%) - High-resolution XPS spectra highlighting the presence of: (b.) In in the form of sulfide and/or oxide ; (c.) O in the form of oxide (∼50%) and ligand (∼50%) ; (d.) S mainly in the form of sulfide (peak at 162 eV). Some is founded to be in a sulfate or sulfonate form ((≤ 10%, peak at 169 eV)

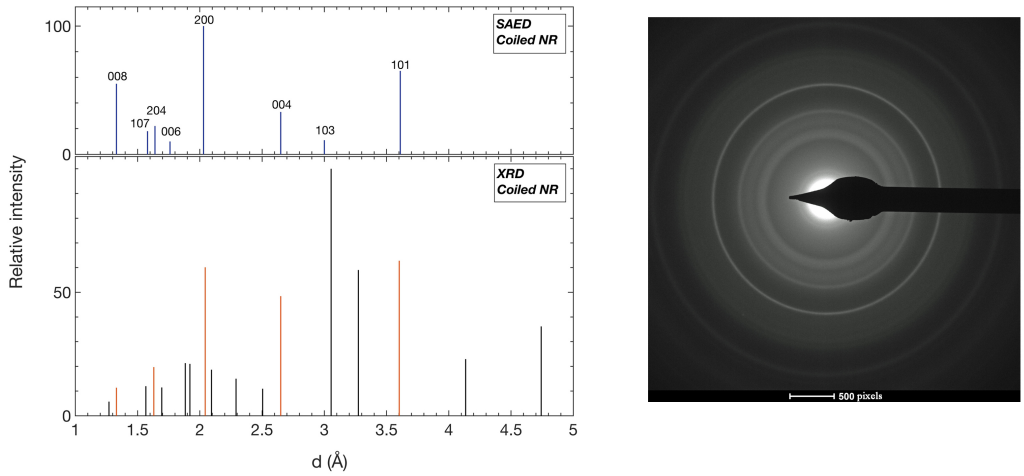

FIG. S5. Left: Interplanar distances measured from SAED (top) compared to interplanar distances calculated from X-ray diffraction (XRD, bottom). From SAED, we were able to select the peaks in the X-ray diffractogram that really correspond to InS NR. We made the attribution according to orthorhombic *Pnnm* InS crystallographic structure (ICDD card n°01-072-0551). Peak in red are those who are shifted after ligand-exchange (see main text). Right: Selected-Area Electron Diffraction (SAED) pattern of InS NR.

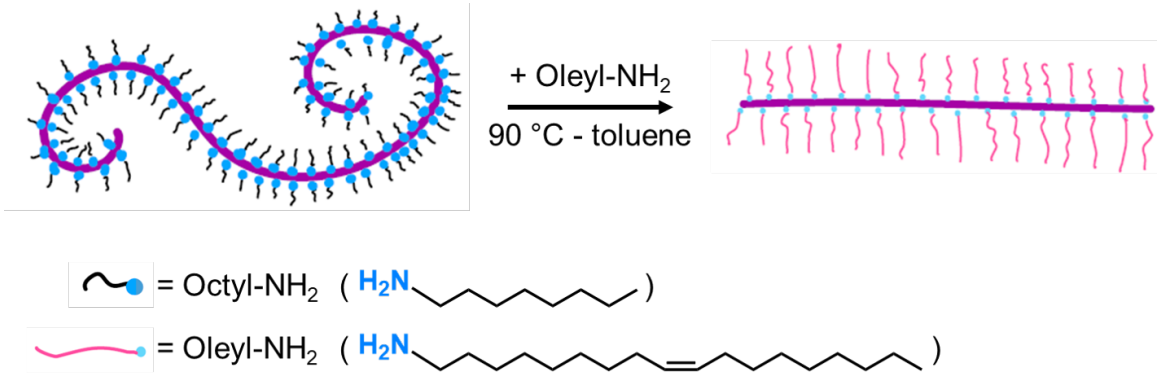

FIG. S6. Representation of the ligand exchange process.

values X values of 4.5 and 9.3 for oleylamine and n-octylamine, respectively. Assuming only one species is bound to the surface of InS NR, TGA results yield surface coverages of 3.5 nm^{-2} and 3.1 nm^{-2} for n-octylamine and oleylamine after ligand exchange and purification, respectively (Fig. S10). Initial n-octylamine-capped NR have a ligand density of 4.3 nm^{-2} (Fig. S9). The lower values of post-exchange ligand densities are explained by purification steps with ethanol after the exchange experiments, which strip off ligands from the NR surface.

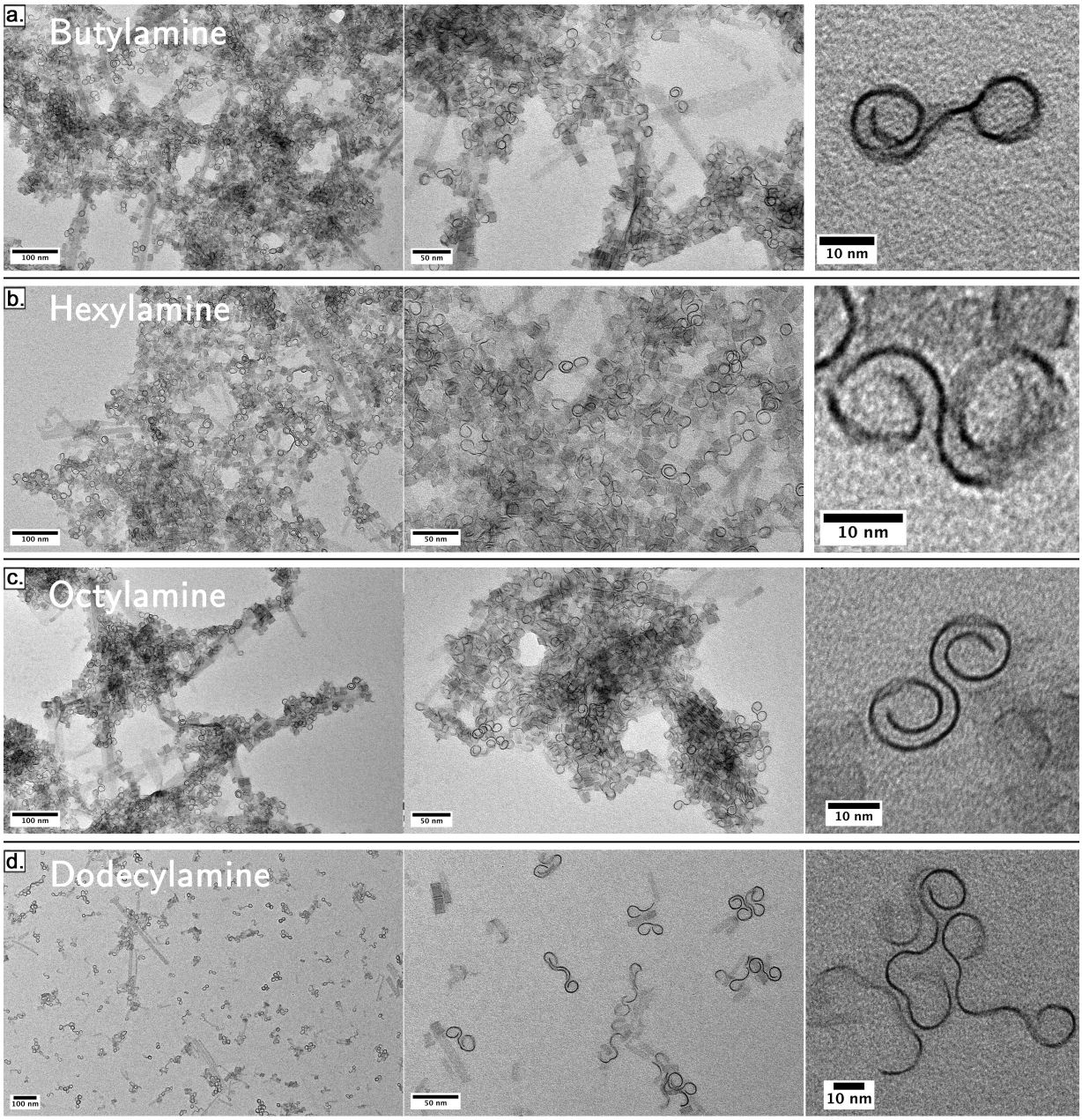

FIG. S7. TEM images of indium sulfide NR TEM capped with : (a.) *n*-butylamine - (b.) *n*-hexylamine - (c.) *n*-octylamine - (d.) *n*-dodecylamine.

C. Surface characterization by NMR spectroscopy

In order to ensure oleylamine is present on the surface of the NR, we performed 1D ^{1}H NMR and diffusion-ordered spectroscopy analyses. First, on samples washed once with absolute ethanol (2/1 v_{EtOH}/v). As shown on Fig. S11, characteristic resonances of oleylamine are detected. However, diffusion experiment gave a diffusion coefficient of $1.07.10^{-9}$ m^2/s which is close to the value of free oleylamine (D = $1.16.10^{-9}$ m^2/s), meaning that the detected signal stems mainly from the remaining free oleylamine.

Unfortunately, when the sample is washed twice with absolute ethanol the NR cannot be resuspended in any of the tested solvent. To overcome this issue, we washed twice the sample using acetone instead of ethanol. As shown on Fig. S12, this sample displays two overlapping signals of oleylamine which could be ascribe to tightly and loosely associated oleylamine.

In this last case, diffusion-ordered spectroscopy analysis in the case of the terminal -CH_3 signal gave a much lower

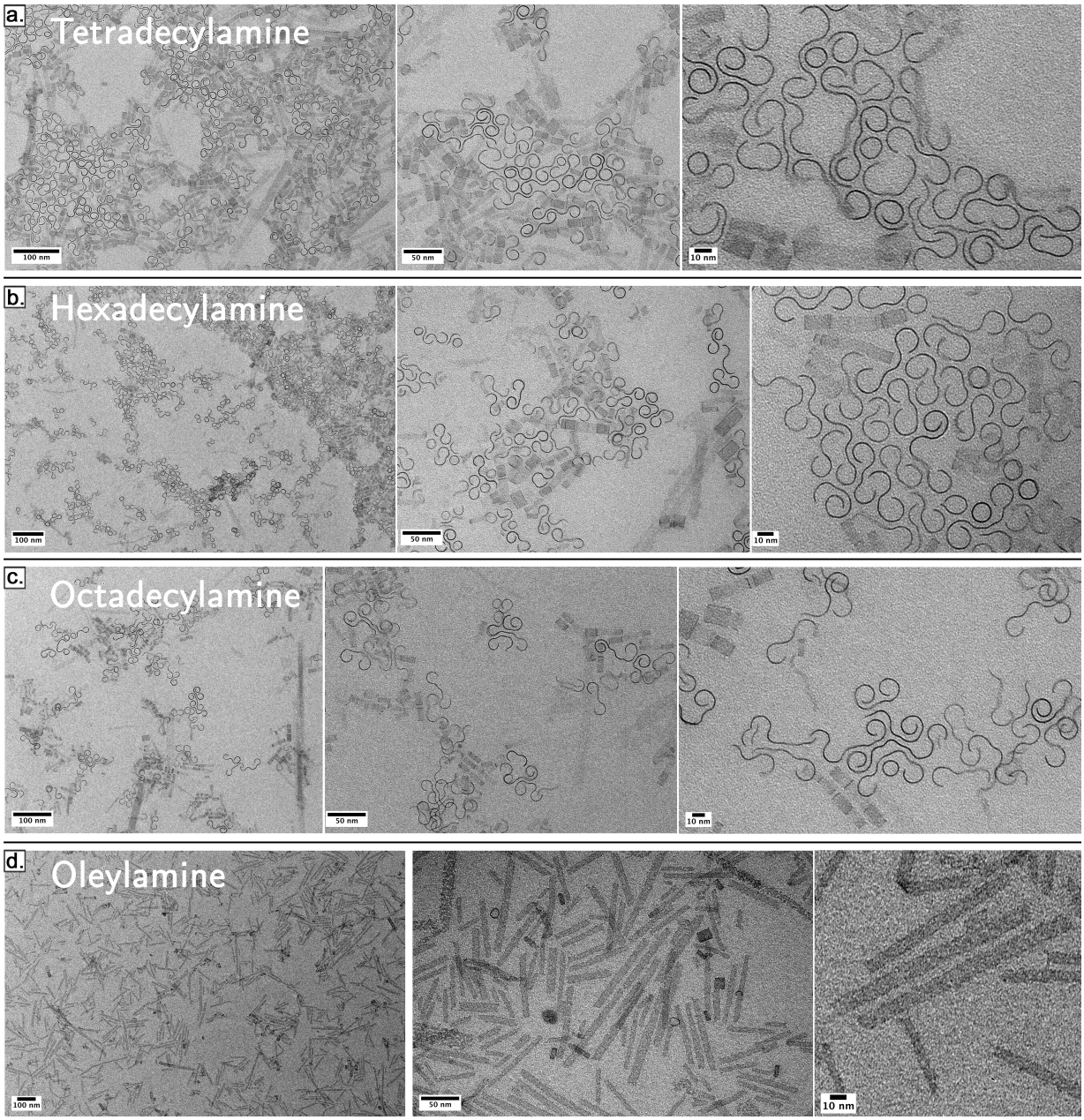

FIG. S8. TEM images of indium sulfide NR TEM capped with : (a.) n-tetradecylamine – (b.) n-hexadecylamine - (c.) n-octadecylamine – (d.) oleylamine.

diffusion coefficient of 8.10^{-10} m^2/s than for free oleylamine (D = $1.16.10^{-9}$ m^2/s). Values obtained for the alkene resonance were too dispersed to be fitted accurately: this might be due to the bivalent nature of this resonance. The low intensity of the alkene resonance can also be attributed to the low amount of materials available for this analysis. Nonetheless, we can conclude that the oleylamine is effectively bound to the InS surface.

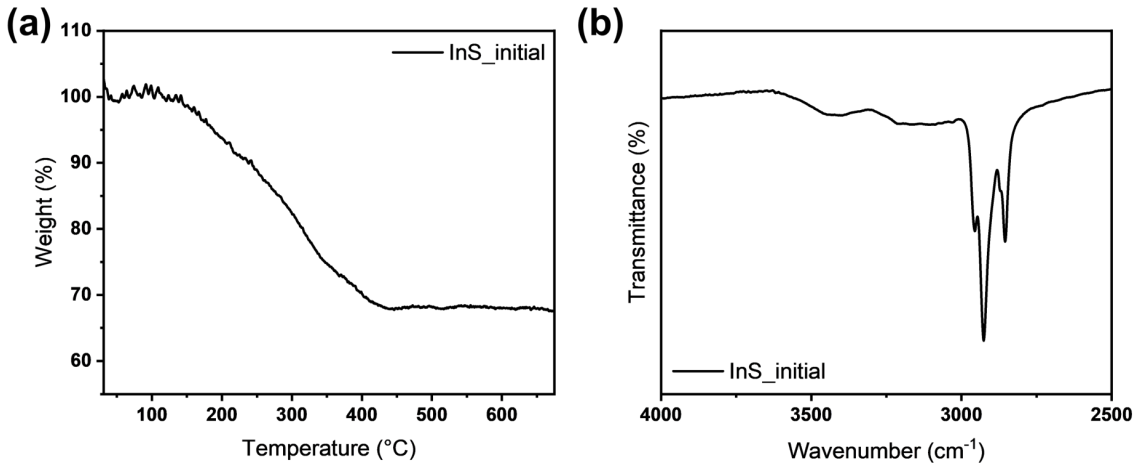

FIG. S9. (a) Thermogravimetric analysis and (b) FT-IR spectrum of InS NR prior to any ligand exchange.

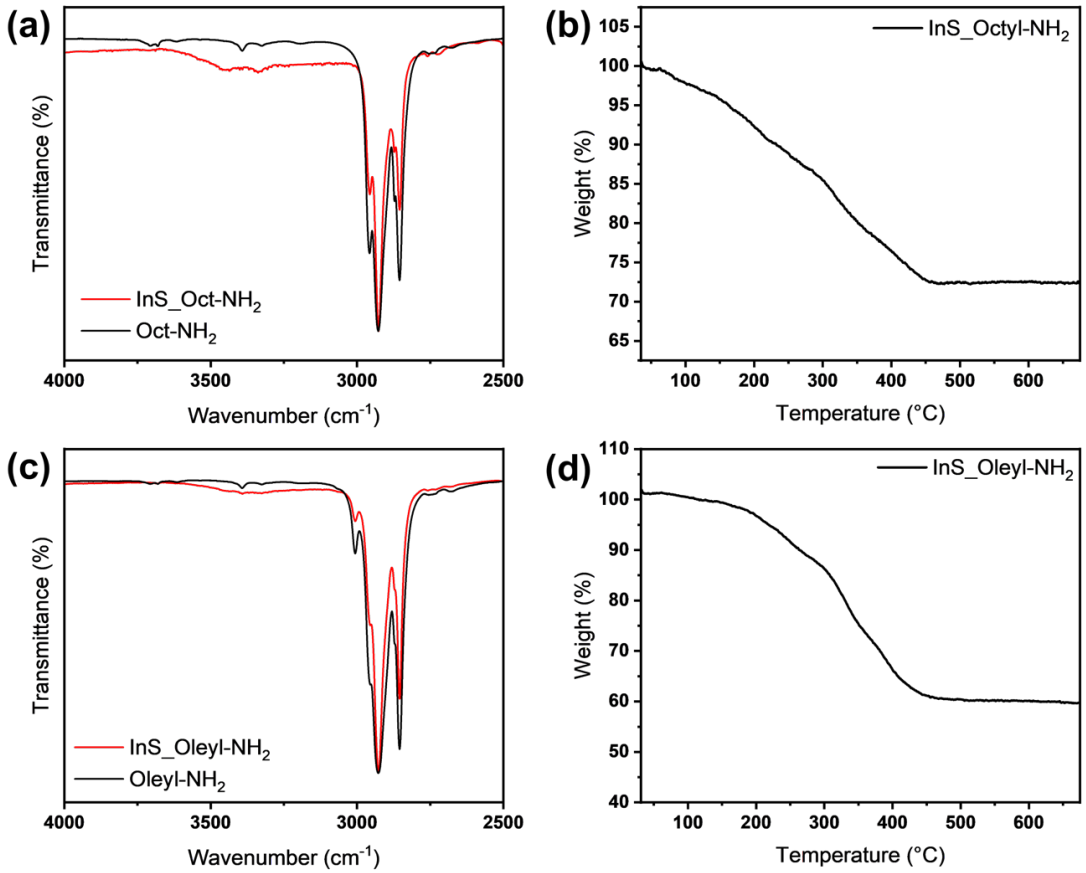

FIG. S10. (a, c) FT-IR spectra of *n*-octylamine and *n*-octylamine-capped InS NR (a), oleylamine and oleylamine-capped InS NR (c). (b, d) Thermogravimetric analysis of *n*-octylamine (b) and oleylamine-capped (d) InS NR, respectively.

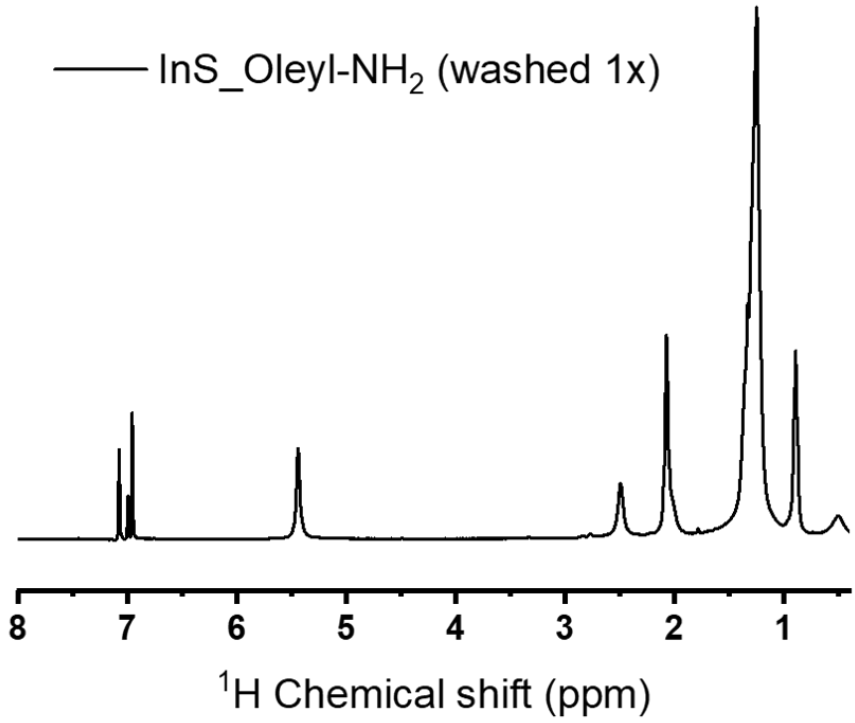

FIG. S11. ^{1}H NMR spectrum of one-time washed InS-Oleyl-NH_2 NR in d_8-toluene.

D. SAXS modeling

As discussed before, TEM images show that ligand-coated NRs roll up to adopt different conformations (see Fig. 1), mainly double spiral-like shapes where the turns are either in the same direction or opposite direction, the latter forming figure-of-eight-like shapes. In addition, numerous partially rolled-up shapes can also be seen, significantly adding to the polydispersity of shapes. Visual inspection clearly shows that the radius of curvature is not constant; rather, it progressively increases or decreases along the ribbon contour. Here, we develop a workflow to extract the average radius of curvature from scattering curves by assuming NRs to form a monodisperse suspension of idealized spirals of a specific type. We calculated the form factors $P(q)$ for four different types of spiral shapes – (i) Archimedean spiral, (ii) Fermat spiral, (iii) logarithmic spiral, and (iv) Cornu's spiral (or clothoid). Out of these four, an analytical expression for $P(q)$ is available in the literature only for logarithmic spirals[50]. Furthermore, visual inspection of rolled-up NRs indicates that their shapes are similar to thin sheets of constant width wrapping around a cylinder. This observation supports the hypothesis that NRs can be suitably modeled as Archimedean spirals, and the other three kinds are not pertinent to our system. We aim to determine whether any distinctive features exist in the form factor that will allow us to determine the parameters of an Archimedean spiral and subsequently calculate its radius of curvature.

Our approach is purely numerical – first, we arranged a set of atoms, which act as idealized point scatterers, in the shape of a ribbon with width 10 nm and a spiral contour of a fixed length L. Then we calculated the orientationally-averaged scattering intensity $I(q)$ from the atomic positions as a function of q and normalized it to obtain $P(q) = I(q)/I(0)$. The atoms were arranged with a uniform spacing of 0.5 nm along both the width and the contour. SAXS being a low-resolution technique, the precise positions of the atoms do not influence the overall scattering patterns. The calculations were performed using the software package Debyer (`https://github.com/wojdyr/debyer`), which

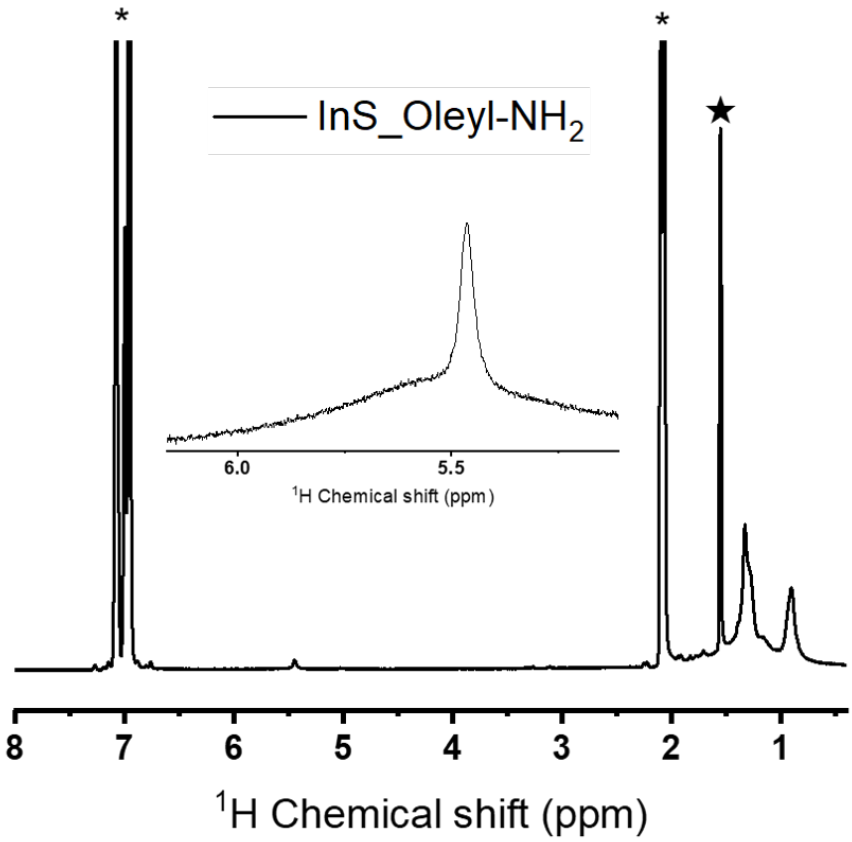

FIG. S12. ^{1}H NMR spectrum of InS-Oleyl-NH_2 NR purified two-times with acetone in d_8-toluene. Signals from toluene ($*$) and acetone ($\star$) are also visible. Insert: zoom in on the alkene region.

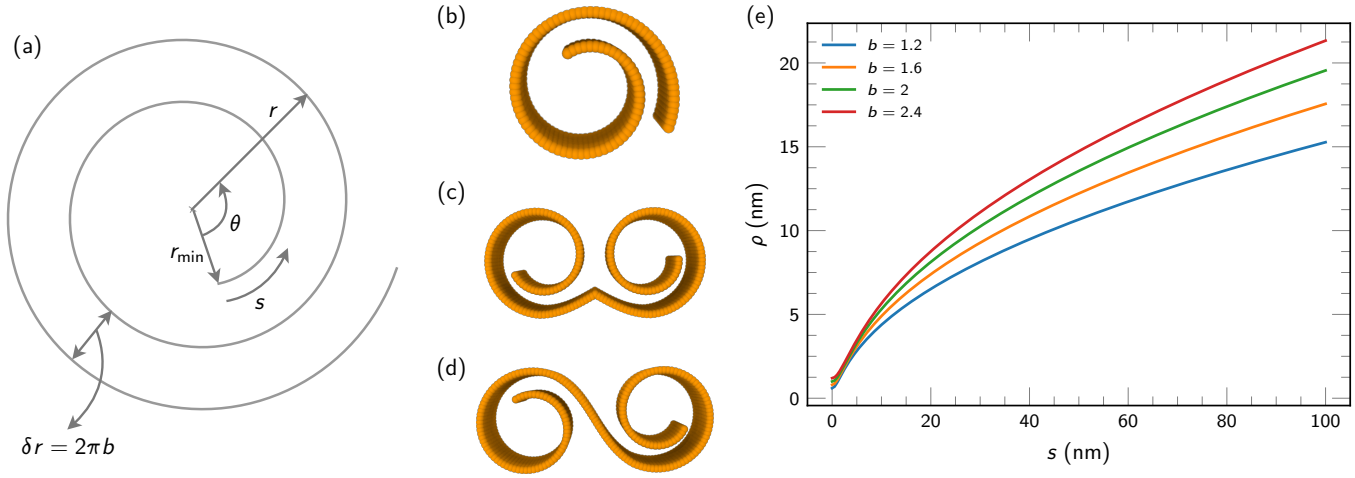

FIG. S13. (a) Graph of an Archimedean spiral indicating all geometric parameters. The arc length s is measured outward along the direction of positive θ. 3D renderings of a single (b) and double spiral with *in/in* (c) and *in/out* (d) conformations. (e) Radius of curvature of single spirals as a function of arc length for different values of the parameter b. In panels (b) – (e) $r_{\min} = 0$.

incorporates a computationally efficient implementation of the Debye scattering formula:

$$I(q) = \sum_{i}^{N} \sum_{j}^{N} f_i f_j \frac{\sin(q r_{ij})}{q r_{ij}}, \tag{3}$$

where f_i is the scattering factor for atom i and r_{ij} is the distance between atoms i and j. In our calculations, we have assumed $f_i = f_j = 1$.

An Archimedean spiral is defined by the polar equation $r = b\theta$, where r is the radius, θ is the polar angle, and b is a parameter (see Fig. S13 (a)). At a fixed θ, the distance between two successive turns $\delta r = 2\pi b$ is constant. The arc length for $\theta_1 \leq \theta \leq \theta_2$ is

$$s = \frac{b}{2} \left[\theta + \sqrt{1 + \theta^2} + \sinh^{-1} \theta \right]_{\theta_1}^{\theta_2}. \tag{4}$$

In addition, another parameter $\mathrm{r_{min}}$ can be introduced which marks the radius at which the curve commences. The primary purpose of $\mathrm{r_{min}}$ is to shift the initial value of θ. Analysis of isolated conformations from the TEM images gives us an estimate of $r_{\mathrm{min}} = 3.62$ nm and $b = 0.47$ nm, though the precise values vary between different conformations.

Two spirals can be joined to form double spirals, where the two curvatures can have the same sign (*in/in* conformation) or opposite sign (*in/out* conformation), as shown in Fig. S13 (c, d). For the *in/in* case, a kink appears in the middle where the two spirals meet. While it is possible to remove the kink, it calls for additional parameters. In Fig. S13(c,d), we have slightly ameliorated the kink by forcing the curvature to linearly attain a value of zero over a small length at the end of each spiral, though the discontinuity in the derivative of curvature still remains. However, for our purposes, the kink turns out to be a minor detail and does not affect our conclusions. The unsigned radius of curvature (for a single spiral) increases with increase in θ following the relation

$$\rho = b \frac{(\theta^2 + 1)^{3/2}}{\theta^2 + 2}. \tag{5}$$

Substituting θ with s, the dependence of ρ on the arc length is shown in Fig. S13(e). The radius of curvature is minimum (curvature is maximum) at the inner edge and increases monotonically toward the outer edge, where the curvature is minimum.

Fig. S14(a) shows the form factors of single spirals of the same contour length but different values of b. A Kratky plot for the same data is shown in Fig. S14(b). The latter exhibits clearly discernable oscillations whose locations vary with b and which are diagnostic of structural features in the scattering objects. For simplicity, we will be concerned only with the locations of the primary oscillation, marked by q^*. For comparison, in Fig. S14(c, d), we present $P(q)$ data for single and double spirals (both *in/in* and *in/out*) of the same contour length at $b = 0.47$ nm. Single spirals show a lower value of q^*, followed by double *in/in* spirals and then by double *in/out* spirals.

In order to compare with measurements of radii of curvature obtained from TEM images, we calculated an average radius of curvature $\tilde{r}$ as the mean of the pointwise radius of curvature along the contour of a spiral. Fig. S15 shows $\tilde{r}$ as a function of q^* for different values of r_{min}.

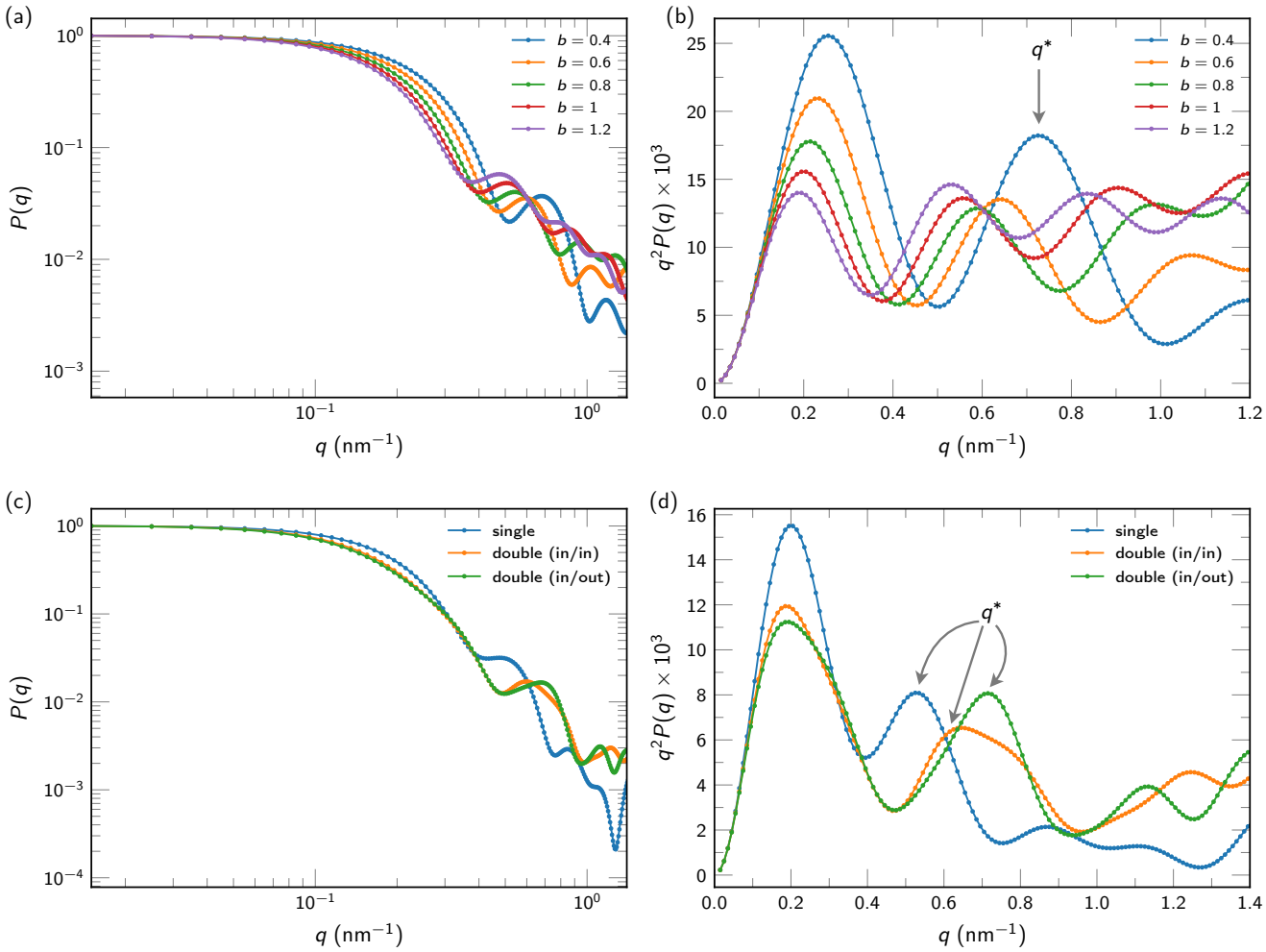

FIG. S14. Form factor (a) and Kratky plot (b) for single spirals with $L = 50$ nm and $r_{\min} = 3.62$ nm for different values of b. The first peak in the Kratky plot for each curve is denoted as q^*. (c) and (d) show corresponding plots at $b = 0.47$ nm for single and double spirals (both *in/in* and *in/out* conformations) with $L = 100$ nm.

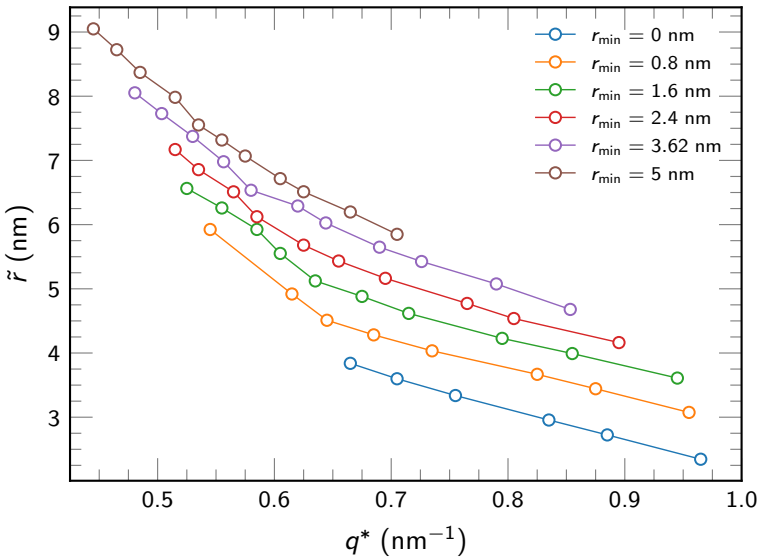

FIG. S15. Average radius of curvature $\tilde{r}$ of single Archimedean sprials as a function of the position of the first peak in Kratky plot q^* for different values of $r_{\min}$. The contour length is 50 nm for all cases.